Polarization Encoded Color Image Embedded in a Dielectric Metasurface

DOI: 10.1002/((please add manuscript number))
Article type: Communication

Polarization Encoded Color Image Embedded in a Dielectric Metasurface

Xiaofei Zang, Fengliang Dong, Fuyong Yue, Chunmei Zhang, Lihua Xu, Zhiwei Song, Ming Chen, Pai-Yen Chen, Gerald S. Buller, Yiming Zhu, Songlin Zhuang, Weiguo Chu*, Shuang Zhang*, Xianzhong Chen*

Prof. Xiaofei Zang, Dr. Fuyong Yue, Chunmei Zhang, Prof. Gerald S. Buller, Prof. Xianzhong Chen
SUPA, Institute of Photonics and Quantum Sciences, School of Engineering and Physical Sciences, Heriot-Watt University, Edinburgh, EH14 4AS, UK
E-mail: x.chen@hw.ac.uk
Prof. Xiaofei Zang, Prof. Yiming Zhu, Prof. Songlin Zhuang
Shanghai Key Lab of Modern Optical System, University of Shanghai for Science and Technology, Shanghai, 200093, China
Dr. Fengliang Dong, Lihua Xu, Zhiwei Song, Prof. Weiguo Chu
Nanofabrication Laboratory, CAS Key Laboratory of Nanosystem and Hierarchical Fabrication, CAS Center for Excellence in Nanoscience, National Center for Nanoscience and Technology, Beijing 100190, China
E-mail: wgchu@nanoctr.cn
Prof. Ming Chen
Center for Photonics Research, Guilin University of Electronic Technology, Guilin 541004, China
Prof. Pai-Yen Chen
Department of Electrical and Computer Engineering, Wayne State University, Detroit, Michigan 48202, USA
Prof. Shuang Zhang
School of Physics and Astronomy, University of Birmingham, B15 2TT
Email: s.zhang@bham.ac.uk

Optical metasurfaces have shown unprecedented capabilities in the local manipulation of the light's phase, intensity and polarization profiles, and represent a new viable technology for applications such as high-density optical storage, holography and display. Here, we demonstrate a novel metasurface platform for simultaneously encoding color and intensity information into the wavelength-dependent polarization profile of a light beam. Unlike typical metasurface devices in which images are encoded by phase or amplitude modulation, the color image here is multiplexed into several sets of polarization profiles, each corresponding to a distinct color, which further allows polarization-modulation induced additive color

mixing. This unique approach features the combination of wavelength selectivity and arbitrary polarization control down to a single subwavelength pixel level. The encoding approach for polarization and color may open a new avenue for novel, effective color display elements with fine control over both brightness and contrast, and may have significant impact for high-density data storage, information security, and anti-counterfeiting.

1. Introduction

Like amplitude and phase, polarization is a fundamental property of light, whose spatial distributions can be used to record, process and store information. However, there are technical challenges in the accurate control of polarization profiles at the subwavelength scale even with the highest quality commercial devices. The traditional polarization manipulation techniques based on birefringence, scattering, specular reflection, and dichroism are usually realized with wave retarders, lenses, spatial phase modulators, and beam splitters, which are large and bulky, thus hindering the large-scale integration of photonic circuits. A vector beam has an inhomogeneous distribution of polarization in the transverse plane perpendicular to the propagation direction. Despite tremendous advances in the fundamental mechanism of vector beams (e.g., Mobius strip [1], Poincare sphere beams [2]), their real-life applications remain scarce, mainly because of the complexity of experimental systems and the inability to control polarization states of light at the subwavelength scale.

Metasurfaces, the two-dimensional counterparts of metamaterials, have provided extraordinary capabilities in local manipulation of the light's amplitude, phase, and polarization, leading to a plethora of novel applications such as generalized Snell's law of refraction[3], Spin-Hall effects[4], flatland metalenses[5], spin-controlled photonics[6], polarization manipulation [7], holograms[8], vortex beam generation[9], and multiplex color router[10]. In addition, the ultrathin nature of metasurface and the ease of fabrication make the metasurface platform very attractive for device miniaturization and system integration. Thus

far, metasufaces have been demonstrated to generate vector beams, such as radially or azimuthally polarized cylindrical beams [11], and arbitrary spatial polarization profiles [12,13]. However, none of the metasurfaces demonstrated previously can be used to encode color images in the polarization profiles. They are also limited by either low efficiency [12] or reflective operation [13] that is not compatible with most optical systems that operate in the transmission mode. Here, we demonstrate a high-efficiency transmissive dielectric metasurface consisting of silicon nanoblocks for realizing control of both polarization and color selectivity, overcoming the above limitations. The approach proposed here can be used to embed a color image, with precisely controlled brightness and contrast, onto a single dielectric metasurface. Unlike previously demonstrated metasurface-based color holograms [14] and full-color printing at the optical diffraction limit [15], here a colorful optical image is encoded in the wavelength-dependent polarization profiles of a light beam. The flexible and controllable generation of arbitrary polarization distributions for light of different colors (wavelengths) with ultracompact metasurfaces may be of interest to many practical applications such as color display, information security, anti-counterfeiting, and high-density information storage.

2. Results

Figure 1a presents a schematic illustration of our proposed approach. Upon the illumination of a linearly polarized light beam with multiple wavelengths, a color image is encoded in the polarization profile the light beam after it passes though the dielectric metasurface and revealed using a linear optical polarizer. The dielectric metasurface consists of silicon nanoblocks "meta-atoms" with different in-plane orientations and sizes on a fused silica substrate, which are used to generate the desired polarization profile for two different colors. The key to realizing a high-resolution color image with spatially-varying intensity mainly lies in the ability of each element to arbitrarily rotate the polarization angle of light in transmission for a particular color, as shown in Figure 1b. In each pixel, a meta-atom functions as an ultracompact half-wave plate that rotates the polarization of linearly polarized light by 2θ (at normal incidence), where θ is the angle between the long side of nanoblock and

the plane of polarization. Therefore, the metasurface can modulate an incident light beam with uniform linear polarization into a vector beam with color-dependent spatially-varying (linear) polarization states. The detailed explanation on the polarization rotation caused by each pixel is given in Supplementary section 1. The resonant wavelength of each silicon nanoblock is dependent on its length (L_x) and width (L_y). As a proof-of-concept, we present here two types of nanoblocks with different lateral dimensions and the same thickness (h=310 nm) along z direction. For silicon nanoblocks with L_x=150 nm and L_y=105 nm, a resonance peak is located around λ=660 nm with a conversion efficiency over 95%. The resonance peak is shifted to λ=550 nm with a conversion efficiency of 80% by changing the structure parameters to L_x=100 nm and L_y=75 nm (see Figure 1c). Here, the conversion efficiency is defined as the ratio between the optical power with desired polarization rotation and the transmitted power. Detailed analysis of the effect of nanoblock shape on polarization purity and diffraction efficiency is given in the Supplementary section 2. By optimizing the dimension and orientation angle of each nanoblock, a light beam with wavelength-dependent polarization profile is generated after passing through the transmissive dielectric metasurface (see the inset of Figure 1a). In order to decode the polarization-encoded high-resolution color image with spatially-varying brightness, an additional linear polarizer (analyzer) is placed behind the metasurface, as shown in Fig. 1a.

To verify the proposed approach, a high-resolution color image of rose with 1200×1200 pixels is selected as a target image for polarization encoding (Figure 2a). Each pixel of the metasurface is 360 nm×360 nm along two perpendicular directions. Figure 2b shows a selected area from the rose with 6×5 pixels (marked with a white square in Figure 2a), which contains both red and green pixels with spatial brightness variation. The corresponding polarization profile of a light beam composed of two different colors is shown in Figure 2c, where the polarization states are represented by red and green arrows, corresponding to wavelengths of 660 nm and 550 nm, respectively. The encoding of the brightness information into the polarization state is based on the Malus' law. Upon the illumination of a linearly polarized light beam generated by a linear optical polarizer, the intensity of the light transmitted through the polarizer (analyzer) is proportional to the square of the cosine of the angle between the transmission axes of the analyzer and the polarizer. Detailed information is

provided in the Supplementary section 3. The desired polarization profiles for different colors are realized by controlling the orientation angles and feature sizes of the nanoblocks (Figure 2d). The corresponding scanning electron microscope (SEM) image of part of the fabricated sample is shown in Figure 2e. The fabrication process and the experiment setup are described in **Experimental Section**.

To characterize the fabricated metasurface device, a tunable supercontinuum laser source (NKT-SuperK EXTREME) is used to provide the incident laser beam with two wavelengths at 550 nm and 660 nm. The sample is mounted on a three-dimensional translation stage, which allows for fine adjustment in all directions. The detailed fabrication process, the material parameters and SEM images of the samples are presented in the Supplementary section 4. In contrast to conventional metasurface-based imaging schemes (e.g., metasurface holograms), here the spatially-varying polarization profile of the modulated light beam cannot be directly observed, since our detectors are not sensitive to the polarization of light. Thus, a specific analyzer (Figure 1a) is required for the acquisition of the image's color and brightness profiles. This feature is potentially useful for anti-counterfeiting and high-density information storage. An objective with a magnification 10× is used to expand the image for visualization with a charge-coupled device (CCD) camera. Since each pixel on the metasurface has a dimension less than the wavelength of incident light, it potentially enables encoding images with a very high resolution. Figures 3a,d show the simulation and experimental results of the revealed image for the incident light beam at the wavelength λ=660 nm. A high-quality image of red flower with a dark background is observed, while the green leaves are missing. The experimental results agree quite well with the numerical simulation, except for a slight discrepancy due to sample imperfection. As is expected, green leaves are captured onto the detector at the wavelength λ=550 nm, as shown in Figure 3e (which agrees with the simulated results depicted in Figure 3b). When a light beam containing two wavelengths (660 nm and 550nm) shines on the metasurface sample, a vivid rose with red

flower and green leaves is revealed as shown in Figure 3c,f. Due to the presence of the brightness information, fine details of the image, such as the petals of the red flowers and the leaf veins are clearly observed. The experimental results at other wavelengths are provided in Supplementary section 5. In stark contrast to the case without analyzer, no image is observed from the transmitted beam (see Supplementary section 6), indicating its great potential for encryption application.

We further show the capability of a properly tailored dielectric metasurface to generate additive color mixing. The primary colors for commonly used additive color mixing are red, green and blue, and white light can be observed if all three overlap in effectively equal mixture. As a proof-of-concept demonstration, we designed two wavelength-selective polarization profiles for producing the polarization-encoded color images based on additive color mixing. Figure 4 shows the schematic illustration of color mixing based on silicon nanoblocks: here, each "supercell" meta-atom contains four nanoblocks of two different types, where two nanoblocks of each type are positioned diagonally. Each supercell responds to a specific wavelength upon the illumination of a light beam containing red and green colors (see Figure 4a). The supercell represents a pixel of a mixed-color image with brightness of each color being individually controlled. The multi-frequency response characteristics of the supercell are given in Supplementary section 7. By controlling the in-plane orientations of the nanoblocks in such a supercell, arbitrary combinations of polarization states (see the double-headed arrows in Figure 4b) for the two colors (red and green) can be generated. Since these two colors are polarization-dependent, the additive color (e.g., a pixel with orange as shown in Figure 4c) can be created by using an analyzer that modulates the ratio between the transmitted intensity of two colors, according to the Malus' Law.

Benefiting from the superior capability of dielectric metasurface in the additive color mixing and the manipulation of local polarization state of light, a multicolor image can be embedded in the polarization profile of a modulated light beam. Here, the transmission axis of

the analyzer is fixed to be perpendicular to that of the linear polarizer for the generation of incident light beams. Figure. 5 shows the simulation and experimental results upon the illumination of linearly polarized red light, green light and their combination. As shown in Figure 5a,d, a good agreement between simulation and experiment is found for the incident light at wavelengths of 660 nm and 550 nm, respectively (also see the experimental demonstrations in Figure 5b,e). When an incident light beam containing two colors (red and green) shines on the fabricated metasurface device, a high-resolution multicolor image composed of eight different types of fruits is revealed (see Figure 5c,f). The minor difference between simulation and experiment is mainly due to the imperfection of sample quality (e.g., nanoblock missing or connected) during the fabrication process and optical measurement system (e.g., misalignment, dust on optical elements). Apart from red and green, other synthetic colors, such as orange, yellow, and dark red, are also observed, which unambiguously demonstrate the color mixing capability of the proposed polarization-encoding approach.

The dielectric metasurface having the ability to encode a spatially-varying and wavelength-selective polarization profile may provide a viable route for generating structured beams that unveil high-resolution color images with well-defined brightness and contrast. In addition, the developed metasurface devices are very robust and can work under the illumination of white continuum light. Experimental results with white light are given in the Supplementary section 8. To evaluate the device performance, we fabricated two metasurfaces consisting of a uniform array of nanoblocks. The measured conversion efficiency and diffraction efficiency are given in the Supplementary section 9. Although the additive color mixing is carried out for only two primary colors (red and green), the proposed approach can be readily extended to three primary colors (red, green and blue) by designing three types of silicon nanoblocks with different feature sizes that respond to the three primary colors (see the supplementary section 10). However, the conversion efficiency for blue light (25% at 460 nm) is lower than that for

red (62% at 660 nm) and green light (55% at 550 nm) due to the material constraint. It is worth mentioning that our metasurface devices are not color holograms - the image is directly imprinted into the polarization distribution of the light beam passing through it, while the design of a hologram involves wavefront (phase) manipulation. In a recently demonstrated polarization-controlled color hologram [16], the color-tunable functionality was realized by controlling the polarization state of the incident light. The device design was based on phase manipulation and the polarization state is uniform across the entire reconstructed image for each color. The reconstructed images could be directly observed under the illumination of light source. In contrast, the image in our work is encoded in the spatially variant phase profile of the light beam, and one needs to indirectly confirm its existence through the decoding process.

3. Conclusion

In summary, we have demonstrated for the first time, the use of dielectric metasurfaces for encoding high-resolution color images with customized brightness profile into the spatially-varying polarization states of light. The dielectric metasurface provides an extraordinary capability in additive color mixing and tailoring the polarization of light at the nanoscale. Our unique approach in color tuning and polarization manipulation may find diverse applications in high-density data storage, information security, and anti-counterfeiting.

4. Experimental Section

Sample Fabrication. Quartz substrates are used to fabricate the designed silicon nanoblocks. First, an amorphous silicon film with a thickness of 310 nm is deposited on the quartz substrate by using an Inductively Coupled Plasma Enhanced Chemical Vapor Deposition System (ICPECVD, Sentech SI 500D). Then, an electron beam evaporator is used to deposit an aluminum film with a thickness of 50 nm, which is used as a charge-dissipation layer and hard mask for etching. The positive electron beam resist (ZEP-520A) with a thickness of 200 nm is spin coated on the sample. After that, nanostructures are defined on the

resist film based on the standard electron-beam lithography (EBL, Vistec EBPG 5000+). The nanopatterns are transferred into the aluminum layer and silicon layer by subsequent etching using an Inductively Coupled Plasma etcher (ICP, Sentech PTSA SI 500). Finally, the silicon nanoblocks are obtained on the quartz substrate by removing the aluminum layer with aluminum etchant.

Experimental setup. The experimental setup for sample characterization is shown in Figure 6. The metasurface samples are exposed to the light from a tunable supercontinuum laser source (NKT-SuperK EXTREME) which provide two colors at the wavelengths of 550 nm and 660 nm. A polarizer with a transmission axis aligned to the y-axis is used to generate the incident light with linear polarization. In order to capture/visualize the image on charge-coupled device (CCD) camera, an objective with magnification of 10× is adopted to expand the image. The analyzer is a linear polarizer with a transmission axis along x-axis, which is used to reveal the encoded color images.

Author Contributions

X.Z., X.C. and S.Z. initiated the idea. X.Z. conducted the numerical simulations. F.D., L.X., Z.S., and W.C. fabricated the samples. X.Z., F.Y., C.Z. and X.C. performed the measurements. X.Z., X.C., S.Z., M.C., P.Y.C., Y.Z., S. Z. and G.S.B. prepared the manuscript. X.C. and W.C. supervised the project. All the authors discussed and analyzed the results.

Acknowledgements

Xiaofei Zang and Fengliang Dong contributed equally to this work. X.C. acknowledges the Engineering and Physical Sciences Research Council of the United Kingdom (Grant Ref: EP/ P029892/1). F.D. and W.C. acknowledge the Youth Innovation Promotion Association CAS (Grant No. 2015030), CAS Key Technology Talent Program, the National Natural Science Foundation of China (Grant No. 11627803) and Key Research Program of Frontier Sciences, CAS (Grant No. QYZDB-SSW-SYS031).

Received: ((will be filled in by the editorial staff))
Revised: ((will be filled in by the editorial staff))
Published online: ((will be filled in by the editorial staff))

References

[1] T. Bauer, P. Banzer, E. Karimi, S. Orlov, A. Rubano, L. Marrucci, E. Santamato, R. W. Boyd, G. Leuchs. *Science* **2015**, *347*, 964.

[2] A. M. Beckley, T. G. Brown, M. A. Alonso. *Opt. Express* **2010**, *18*, 10777.

[3] a) N. F. Yu, P. Genevet, M. A. Kats, F. Aieta, J. P. Tetienne, F. Capasso, Z. Gaburro. *Science* **2011**, *334*, 333; b) X. Ni, N. K. Emani, A. V. Kildishev, A. Boltasseva, V. M. Shalaev. *Science* **2012**, *335*, 427; c) L. Huang, X. Chen, H. Mühlenbernd, G. Li, B. Bai, Q. Tan, G. Jin, T. Zentgraf, S. Zhang. *Nano Lett.* **2012**, *12*, 5750; d) S. Sun, Q. He, S. Xiao, Q. Xu, Q. X. Li, L. Zhou. *Nat. Mater.* **2012**, *11*, 426.

[4] X. Yin, Z. Ye, J. Rho, Y. Wang, X. Zhang, *Science* **2013**, *339*, 1405.

[5] a) X. Chen, L. Huang, H. Mühlenbernd, G. Li, B. Bai, Q. Tan, G. Jin, C. Qiu, S. Zhang, T. Zentgraf. *Nat. Commun.* **2012**, *3*, 1198; b) S. M. Wang, P. C. Wu, V.-C. Su, Y.-C. Lai, C. H. Chu, J.-W. Chen, S.-H. Lu, J. Chen, B. B. Xu, C.-H. Kuan, T. Li, S. N. Zhu, and D. P. Tsai, *Nat. Commun.* **2017**, *8*, 187.

[6] a) N. Shitrit, I. Yulevich, E. Maguid, D. Ozeri, D. Veksler, V. Kleiner, E. Hasman. *Science* **2013**, *340*, 724; b) J. Lin, M. J. P. B. Mueller, Q. Wang, G. Yuan, N. Antoniou, X. Yuan, F. Capasso. *Science* **2013**, *340*, 331; c) D. Wen, S. Chen, F. Yue, K. Chan, M. Chen, M. Ardron, K. Li, P. Wong, K. Cheah, E. Pun, G. Li, S. Zhang, X. Chen. *Adv. Opt. Mater.* **2016**, *4*, 321.

[7] a) N. Yu, F. Aieta, P. Genevet, M. A. Kats, Z. Gaburro, F. Capasso. *Nano Lett*. **2012**, *12*, 6328; b) N. K. Grady, J. E. Heyes, D. R. Chowdhury, Y. Zeng, M. T. Reiten, A. K. Azad, A. J. Taylor, D. A. R. Dalvit, H. T. Chen. *Science* **2013**, *340*, 1304; c) P. C. Wu, W.-Y Tsai, W. T. Chen, Y.-W. Huang, T.-Y. Chen, J.-W. Chen, C. Y. Liao, C. H. Chu, G. Sun,

D. P. Tsai. *Nano. Lett.* **2017**, *17*, 445; d) D. Wen, F. Yue, C. Zhang, X. Zang, H. Liu, W. Wang, X. Chen, *Appl. Phys. Lett.* **2017**, 111, 023102.

[8] a) X. Ni, A. V. Kildishev, V. M. Shalaev. *Nat. Commun.* **2013**, *4*, 2807; b) L. Huang, X. Chen, H. Mühlenbernd, H. Zhang, S. Chen, B. Bai, Q. Tan, G. Jin, K. Cheeah, C. Qiu, J. Li, T. Zentgraf. S. Zhang. *Nat. Commun.* **2013**, *4*, 2808; c) G. Zheng, H. Mühlenbernd, M. Kenney, G. Li, T. Zentgraf, S. Zhang. *Nat Nanotechnol***. 2015**, *10*, 308; d) D. Wen, D. F. Yue, G. Li, G. Zheng, K. Chan, S. Chen, M. Chen, K. F. Li, P. W. H. Wong, K. W. Cheah, E. Y. B. Pun, S. Zhang, X. Chen. *Nat. Commun.* **2015**, *6*, 8241; e) W. T. Chen, K. Y. Yang, C. M. Wang, Y. W. Huang, G. Sun, I. Chiang, C. Y. Liao, W. L. Hsu, H. T. Lin, S. L. Sun, L. Zhou, A. Q. Liu, D. P. Tsai. *Nano. Lett.* **2014**, *14*, 225; f) H.-H. Hsiao, C. H. Chu, D. P. Tsai. *Small Methods* **2017**, *1*, 1600064.

[9] a) E. Karimi, S. A. Schulz, I. D. Leon, H. Qassim, J. Upham, R. W. Boyd. *Light Sci. Appl.* **2014**, *3*, e167; b) M. Pu, X. Li, X. Ma, Y. Wang, Z. Zhao, C. Wang, C. Hu, P. Gao, C. Huang, H. Ren, X. Li, F. Qin, J. Yang, M. Gu, M. Hong, X. Luo. *Sci. Adv*. **2015**, *1*, e1500396; c) M. Q. Mehmood, S. Mei, S. Hussain, K. Huang, S. Y. Siew, L. Zhang, T. Zhang, X. Ling, H. Liu, J. Teng, A. Danner, S. Zhang, C. Qiu. *Adv. Mater.* **2016**, *28*, 2533; d) F. Yue, D. Wen, C. Zhang, B. D. Gerardot, W. Wang, S. Zhang, X. Chen. *Adv. Mater*. **2017**, *29*, 1603838.

[10] B. H. Chen, P. C. Wu, V.-C. Su, Y.-C. Lai, C. H. Chu, I. C. Lee, J.-W. Chen, Y. H. Chen,Y.-C. Lan, C.-H. Kuan, D. P. Tsai. *Nano Lett.* **2017**, *17*, 6345.

[11] F. Yue, D. Wen, J. Xin, B. D. Gerardot, J. Li, X. Chen. *ACS Photon.* **2016**, *3*, 1558.

[12] L. Wang, T. Li, R. Y. Guo, W. Xia, X. G. Xu, S. N. Zhu. *Sci. Rep.* **2013**, *3*, 2603.

[13] F. Yue, C. Zhang, X. Zang, D. Wen, B. D. Gerardot, S. Zhang, X. Chen. *Light: Sci & Appl*. **2018**, *7*, e17129 .

[14] a) Y. W. Huang, W. T. Chen, W. Tsai, P. Wu, C. Wang, G. Sun, D. P. Tsai. *Nano. Lett.* **2015**, *15*, 3122; b) X. Li, L. Chen, Y. Li, X. Zhang, M. Pu, Z. Zhao, X. Ma, Y. Wang, M.

Hong, X. Luo. *Sci. Adv.* **2016**, *2*, e1601102; c) W. Wan, J. Gao, X. Yang. *ACS Nano* **2016**, *10*, 10671; d) B. Wang, F. Dong, Q. T. Li, D. Yang, C. Sun, J. Chen, Z. Song, L. Xu, W. Chu, Y. F. Xiao, Q. Gong, Y. Li. *Nano. Lett*. **2016***, 16*, 5235.

[15] a) K. Kumar, H. Duan, R. S. Hegde, S. C. Koh, J. N. Wei, J. K. Yang. *Nat. Nano.* **2012**, *7*, 557; b) X. M. Goh, Y. Zheng, S. J. Tan, L. Zhang, K. Kumar, C. W. Qiu, J. K. Yang. *Nat. Commun.* **2014,** 5, 5361; c) X. M. Goh, Y. Zheng, S. J. Tan, L. Zhang, K. Kumar, C. W. Qiu, J. K. Yang. *Nano. Lett.* **2014,** *14,* 4023; d) X. Zhu, W. Yan, U. Levy, N. A. Mortensen, A. Kristensen. *Sci. Adv.* **2017**, *3*, e1602487.

[16] B. Wang, F. Dong, D. Yang, Z. Song, L. Xu, W. Chu, Q. Gong, Y. Li, *Optica* **2017**, *4*, 1368.

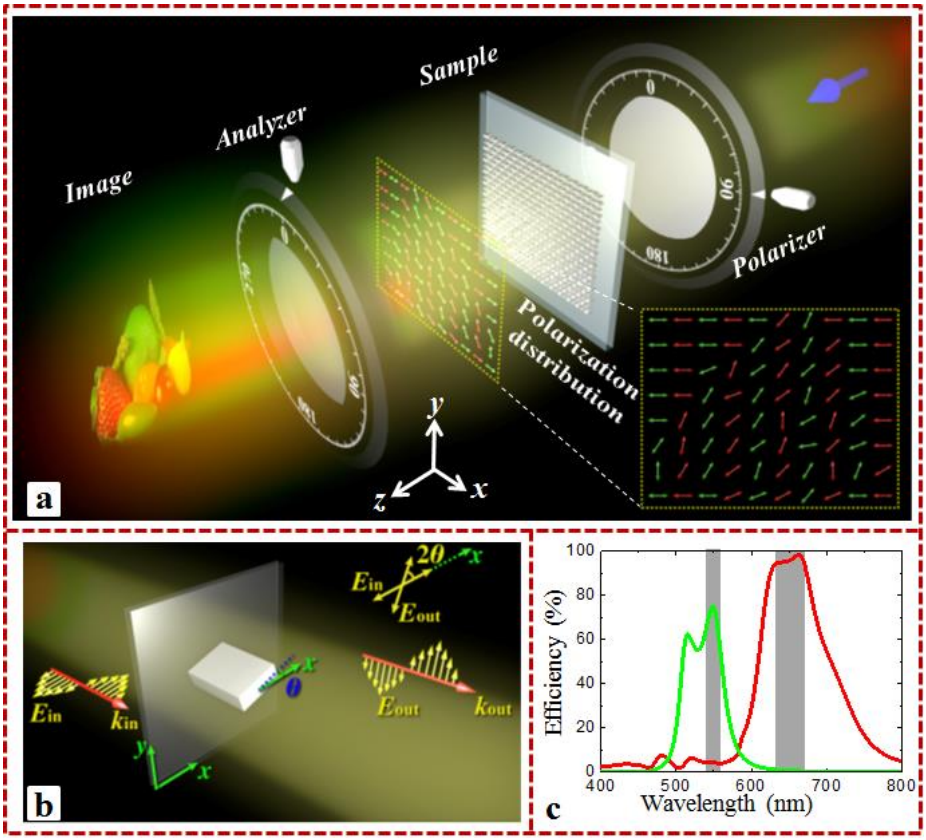

Fig. 1. Schematics for the polarization encoded color image and calculated conversion efficiency of silicon nanoblocks. (**a**) Schematic of polarization encoding and decoding setup. A linear polarizer with a transmission axis along the *x* axis is used to generate the the linearly polarized dual-wavelength laser beam (550 nm and 660 nm), which shines on the transmissive dielectric metasurface. The required spatially variant polarization states for two colors are generated after the incident light beam passes through the sample. The red and green arrows with various directions represent the variety of the polarization states for the light with red and green colors. The encoded fruity combos are revealed after the resultant light beam from the metasurface passing through an analyzer (linear polarizer) with a transmission axis along the vertical direction. (**b**) Schematic of the polarization rotating based on a single nanoblock. The transmissive dielectric metasurface consists of silicon nanoblocks with spatially-variant orientations and different dimensions. Upon the illumination of a linearly polarized light along *x* direction, the polarization direction of the transmitted light beam is rotated counterclockwise with 2θ by a silicon nanoblock with an orientation angle θ with respect to *x* axis. Each nanoblock with a certain orientation angle can rotate the linear polarization of the incident light, providing a tool to realize spatially-variant polarization states for image encoding. (**c**)The calculated conversion efficiency for nanoblocks with L_x=150 nm, L_y=105 nm (red line); L_x=100 nm, L_y=75 nm (green line). The height and period of both types of the nanoblocks are 310 nm and 360 nm, respectively.

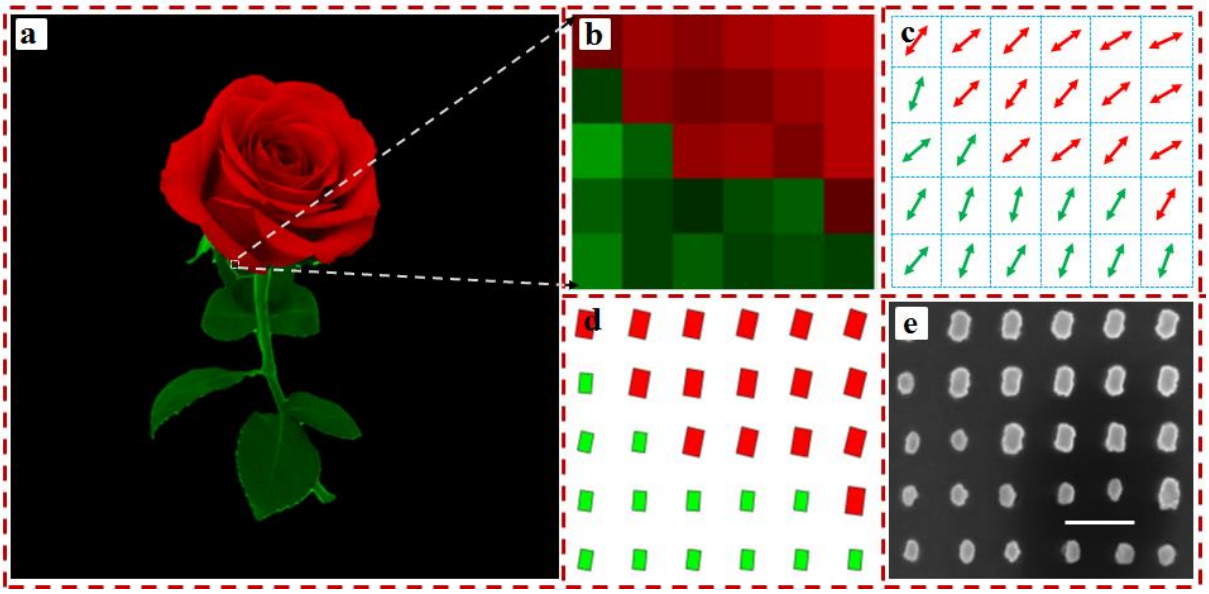

Fig. 2. Mechanism of the polarization encoded color image. (**a**) The target image of the red rose with green leaves. (**b**) An selected area from the rose (see the white square area in (**a**)) with 6×5 pixels, in which it contains both red and green pixels with different gray level. (**c**) The desired polarization distribution for encoding the detail of the selected area (see (**b**)) when the analyer with a transmission axis is along the vertical direction. The red and green arrows show the wavelength-dependent polarization distributions. (**d**) The corresponding nanoblock dirtributions of metasurfaces for the polarization generation in (**c**). (**e**) The SEM image of the fabricated sample. The scale bar is 500 nm.

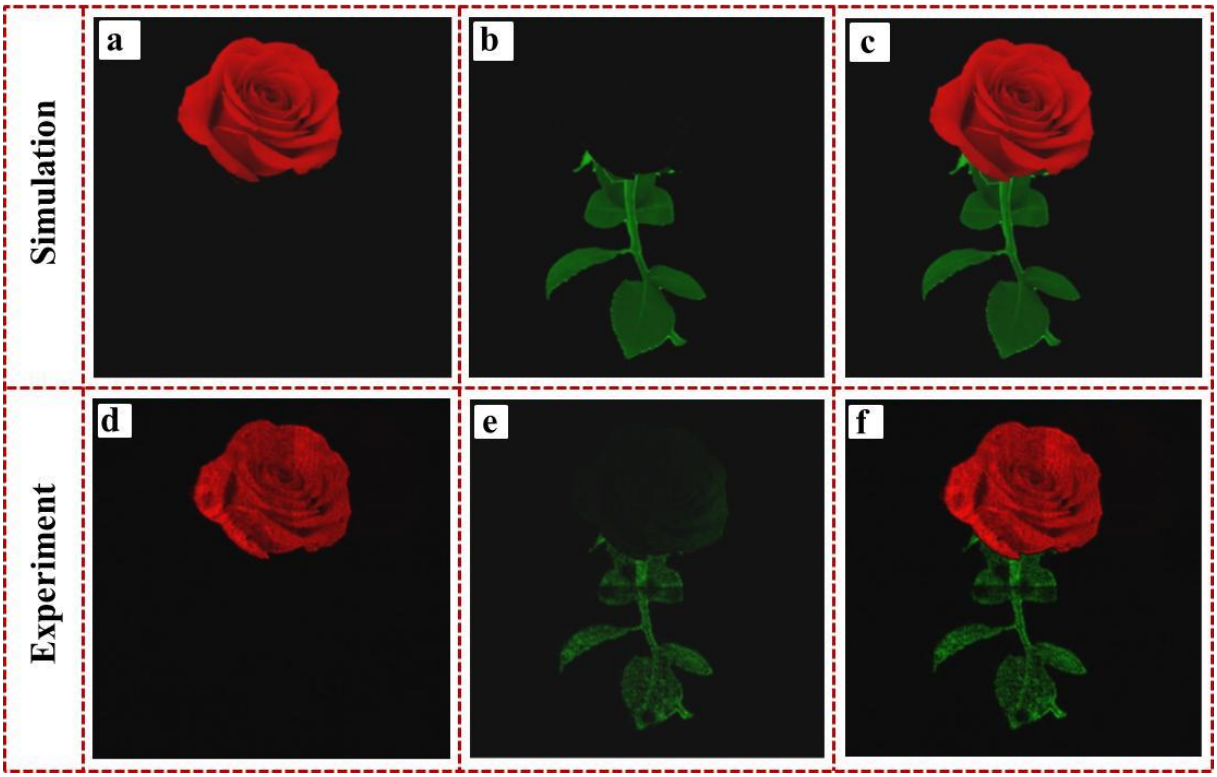

Fig. 3. Simulated and experimental results of the polarization encoded color image. The revealed color image when illuminated with light at the wavelengths (a) and (d) λ=660 nm; (b) and (e) λ=550 nm; (c) and (f) λ=660 nm and 550 nm. The images in the first row and second row represent the simulated and experimental results, respectively.

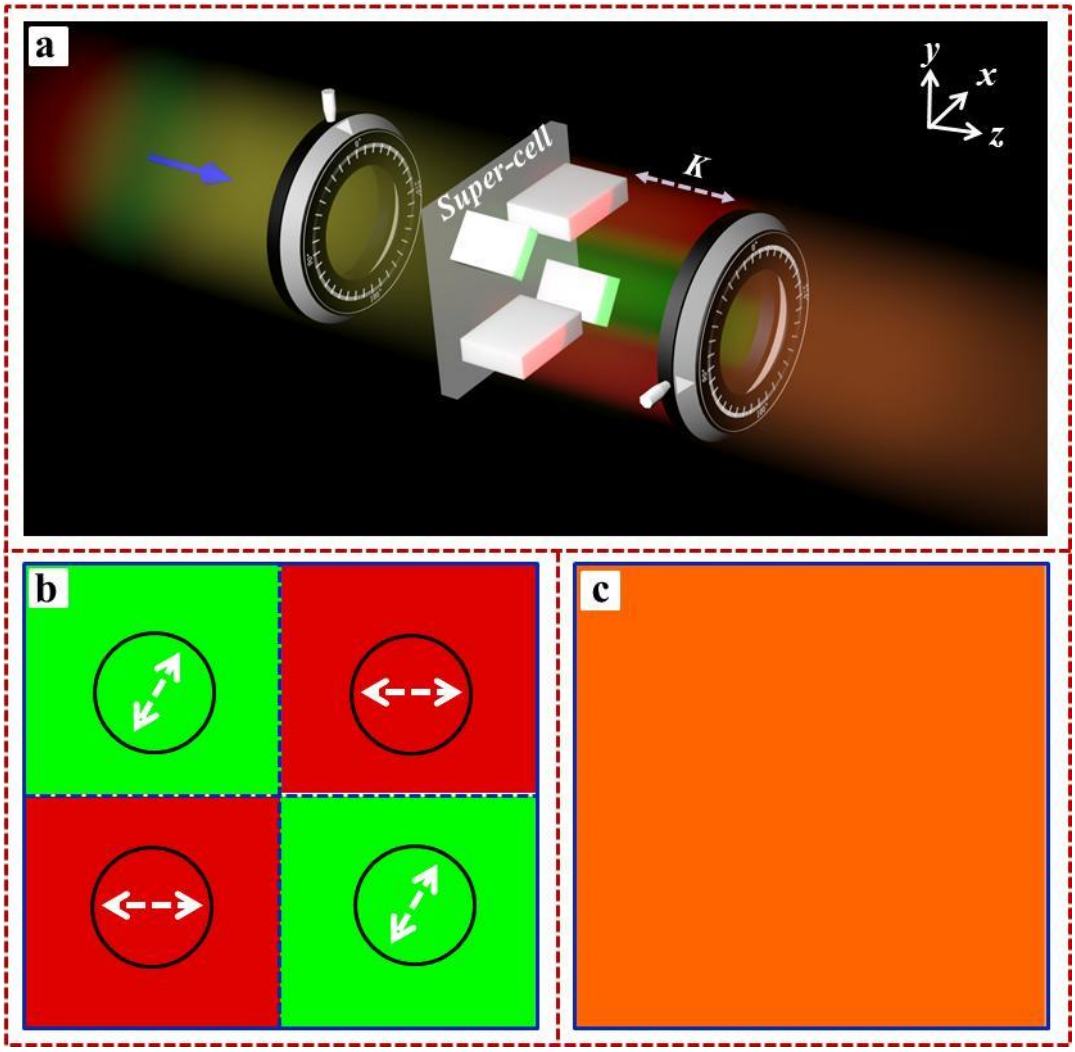

Fig. 4. Mechanism of additive color mixing in a supercell. (**a**) A vertically polarized dual-wavelength light beam containing red and green colors impinges on a supercell consisting of four nanoblocks, including two identical nanoblocks in the diagonal direction. The transmission axis of the analyzer is perpendicular to that of the linear polarizer for the generation of incident light with linear polarization. (**b**) The polarization distribution (arrows in each subcell) of the transmitted light beam after the incident light passing through the supercell (in region K of (**a**)). (**c**) A new color is generated based on the polarization states for two different colors in (**b**).

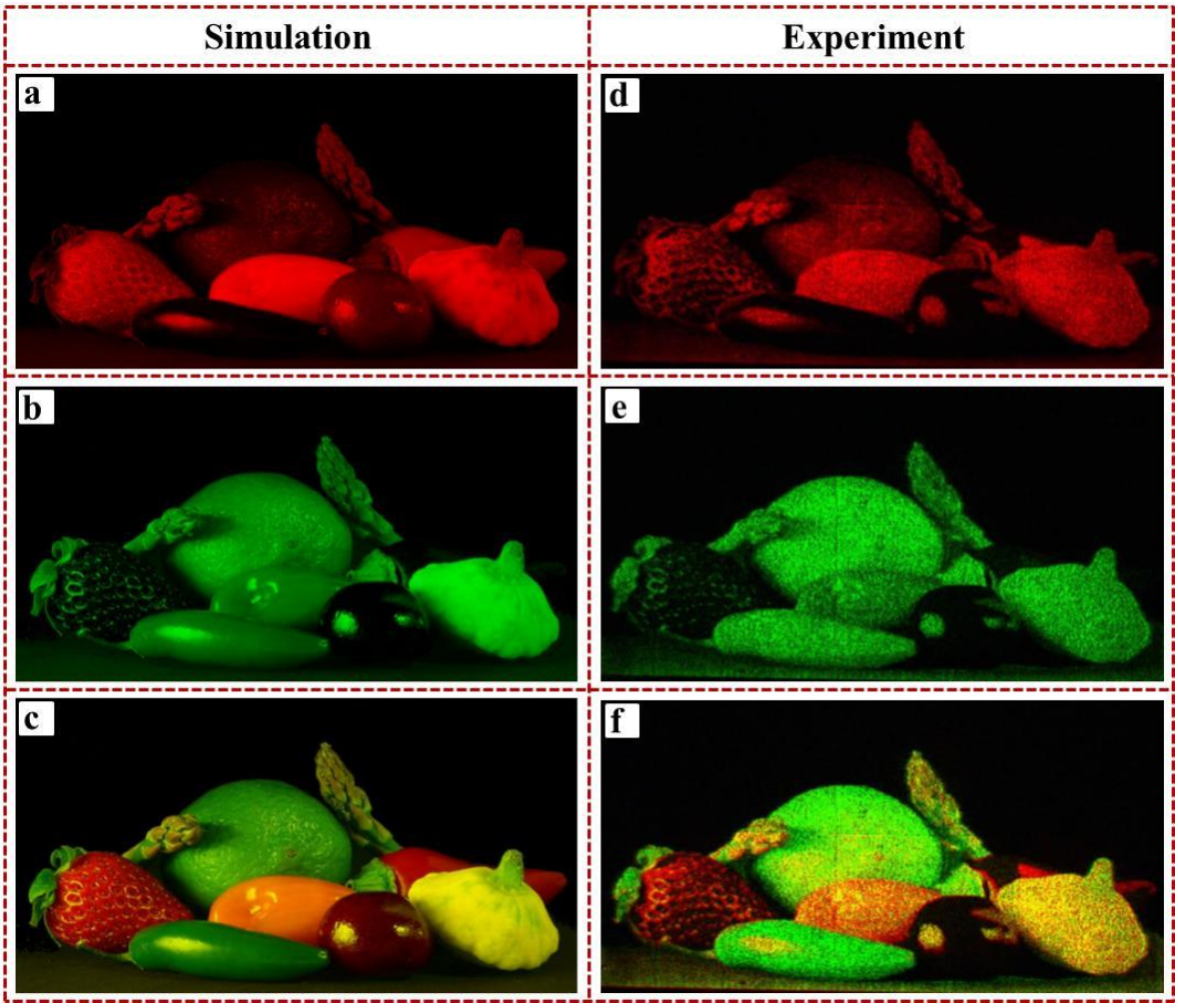

Fig. 5. Simulated and experimental results of the full-color-like image. (**a**) and (**d**) for the revealed image under the illumination of red light beam (λ=660nm), while (**b**) and (**e**) are the cases with the green light beam illumination (λ=550nm). (**c**) and (f) are the full-color-like image with the incidence of both red and green light. The images in the first row and second row represent the simulated and experimental results, respectively.

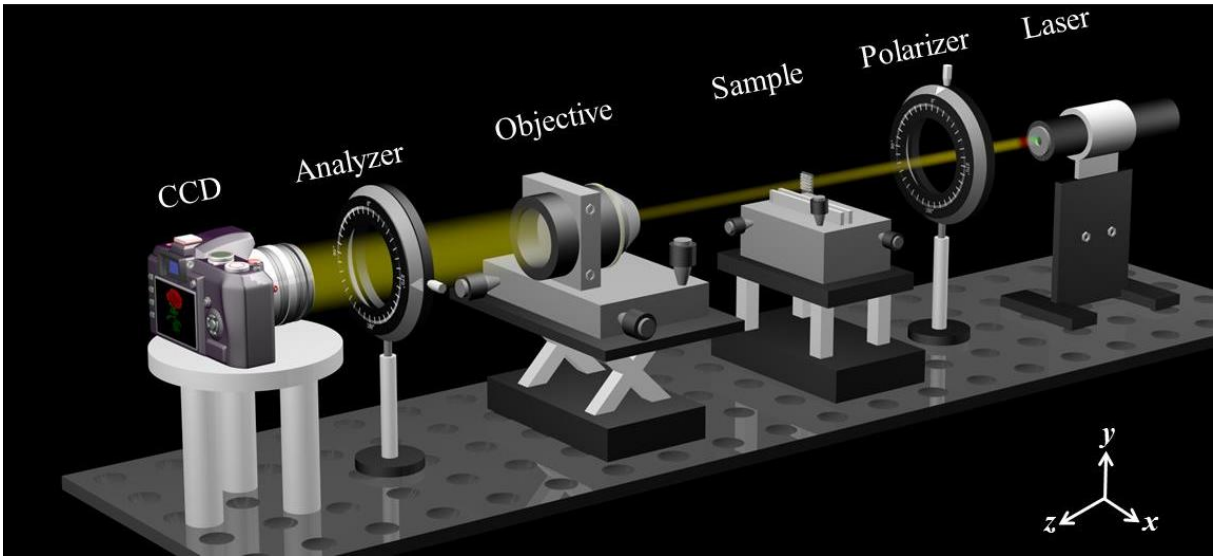

Fig. 6. Experimental setup. A polarizer is used to generate a *y*-polarized dual-wavelength light beam, which is normally incident on the sample. An objective with a magnification of 10× is used to expand the image. An analyer with a transmission axis aligned to the *x*-axis is used to reveal the encoded high-resolution image, which is collected by a CCD camera.

A novel metasurface platform is proposed and experimentally demonstrated to simultaneously encode color and intensity information into the wavelength-dependent polarization profile of a light beam. This unique approach features the combination of wavelength selectivity and arbitrary polarization control down to a single subwavelength pixel level. A linear polarizer is required for the acquisition of the image's color and brightness profiles.

Keywords: Metasurface, polarization control, vector beam, color mixing

Xiaofei Zang, Fengliang Dong, Fuyong Yue, Chunmei Zhang, Lihua Xu, Zhiwei Song, Ming Chen, Pai-Yen Chen, Gerald S. Buller, Yiming Zhu, Songlin Zhuang, Weiguo Chu*, Shuang Zhang*, Xianzhong Chen*

Title: Polarization Encoded Color Image Embedded in a Dielectric Metasurface

ToC Figure

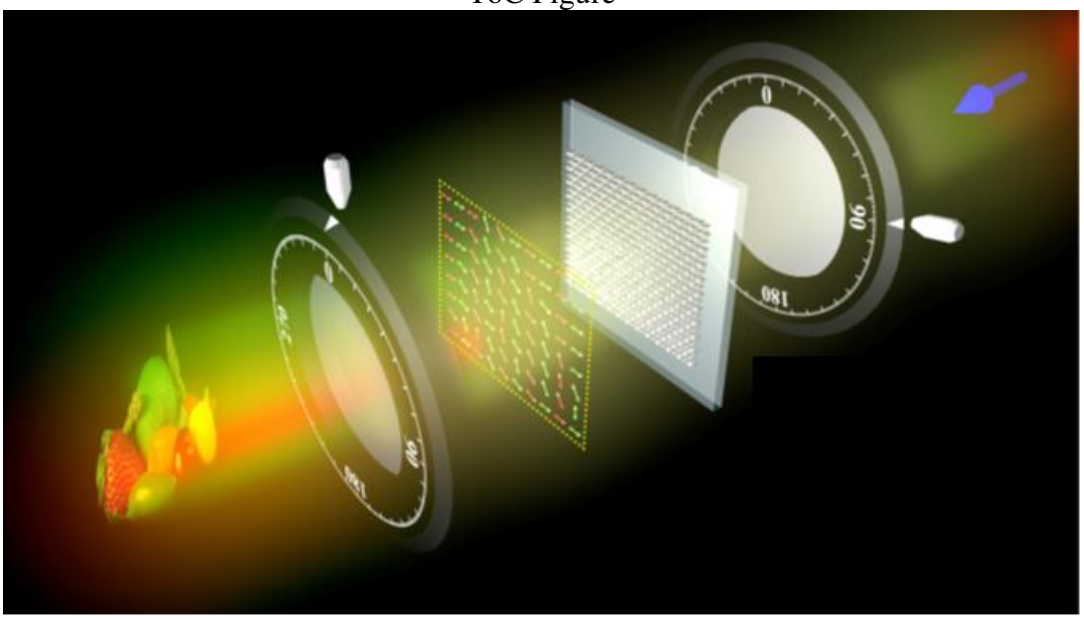

Supporting Information

Polarization Encoded Color Image Embedded in a Dielectric Metasurface

Xiaofei Zang, Fengliang Dong, Fuyong Yue, Chunmei Zhang, Lihua Xu, Zhiwei Song, Ming Chen, Pai-Yen Chen, Gerald S. Buller, Yiming Zhu, Songlin Zhuang, Weiguo Chu*, Shuang Zhang*, Xianzhong Chen*

Section 1. Theory of polarization rotating states embedded in a light beam

Fig. S1 (A) illustrates the schematic of the linear polarization rotation. The Jones matrix of a silicon nanoblock with in-plane orientation angle of θ can be expressed as[R1]:

$$T(\theta) = R(-\theta)T_0(\theta) = \begin{bmatrix} \cos\theta & -\sin\theta \\ \sin\theta & \cos\theta \end{bmatrix} \begin{bmatrix} i\sqrt{\xi(\lambda)} & 0 \\ 0 & -i\sqrt{\xi(\lambda)} \end{bmatrix} \begin{bmatrix} \cos\theta & \sin\theta \\ -\sin\theta & \cos\theta \end{bmatrix} = i\sqrt{\xi(\lambda)} \begin{bmatrix} \cos 2\theta & \sin 2\theta \\ \sin 2\theta & -\cos 2\theta \end{bmatrix}, \quad (1)$$

where T_0 represents the Jones matrix of the silicon nanoblock without rotation, and R(θ) is the rotator operator. $\xi(\lambda)$ is the conversion efficiency. For a linearly polarized light beam along the horizontal direction, it can be decomposed into a LCP light beam and a RCP light beam with equal intensities and zero initial phase. When a linearly polarized light beam along the horizontal direction shines on the nanoblock (see Fig. S1), the LCP light beam is partially converted into RCP light beam with an additional phase delay 2θ while the RCP light beam is partially converted into its opposite helicity with an additional phase delay -2θ. The corresponding transmitted electric field for each converted Note can be expressed as follows:

$$E_{LCP/RCP} = i\sqrt{\frac{\xi(\lambda)}{2}} e^{\pm i2\theta} \begin{bmatrix} 1 \\ \mp i \end{bmatrix} \quad (2)$$

Since the converted parts have the same intensities and the opposite helicity, they are combined into a linearly polarized light beam. It can be written as follows:

$$E_{con} = i\sqrt{\frac{\xi(\lambda)}{2}} e^{-i2\theta} \begin{bmatrix} 1 \\ i \end{bmatrix} + i\sqrt{\frac{\xi(\lambda)}{2}} e^{i2\theta} \begin{bmatrix} 1 \\ -i \end{bmatrix} = i\sqrt{\frac{\xi(\lambda)}{2}} \begin{bmatrix} \cos(2\theta) \\ \sin(2\theta) \end{bmatrix}, \quad (3)$$

This leads to the polarization rotation of 2θ for the converted linearly polarized light beam. If there are various nanoblocks with different in-plane orientations on the metasurface (see Fig. S1(b)), a homogeneously incident light beam with linear polarization is converted into an

inhomogeneous polarization profile of the light beam, providing the desired polarization-rotating states for image encoding, as shown in Fig. S1(c).

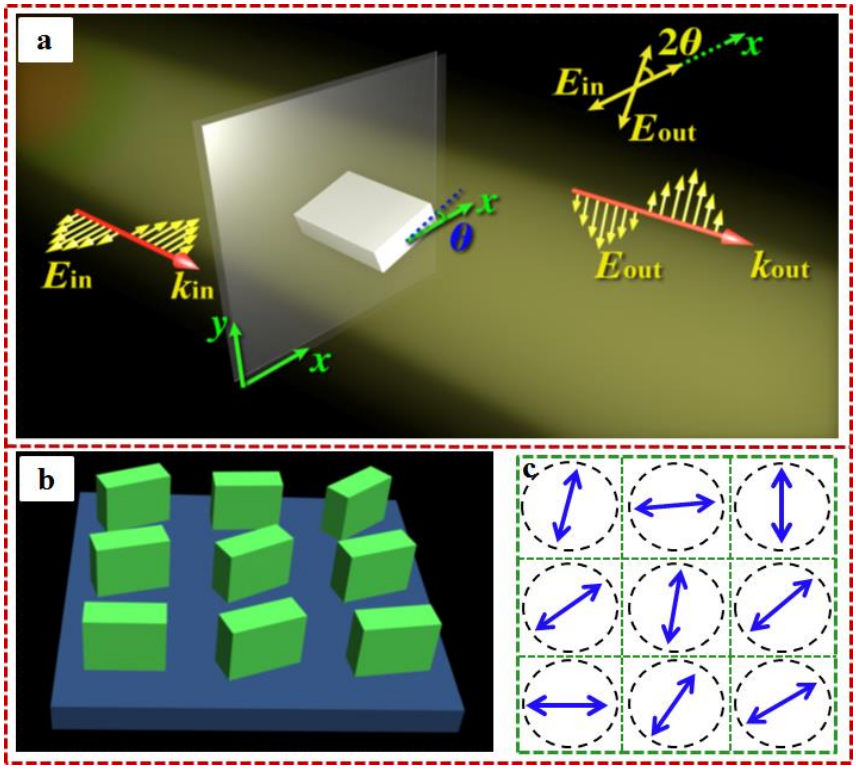

Figure S1. Polarization rotation generated by the dielectric metasurface. (a)The polarization of a linearly polarized light beam is rotated by 2θ counterclockwise after passing through a nanoblock with in-plane orientation angle of θ. (b) nine nanoblocks with different in-plane orientations on the metasurface can generate nine corresponding polarization states (c).

Section 2. Effects of the nanoblock shape on conversion efficiency and diffraction efficiency

Device performance (e.g., polarization purity and diffraction efficiency) is affected by the sample imperfection (e.g., nanoblock shape in Fig. S2) due to the fabrication error. The conversion efficiency (polarization purity) is defined as the ratio between the optical power with desired polarization rotation and the transmitted power, while the diffraction efficiency is the ratio between the optical power with desired polarization rotation and the incident power [R3]. Fig. S3 and Fig. S4 show the effect of silicon nanoblock shape on the conversion efficiency and diffraction efficiency for red and blue color filtering, respectively.

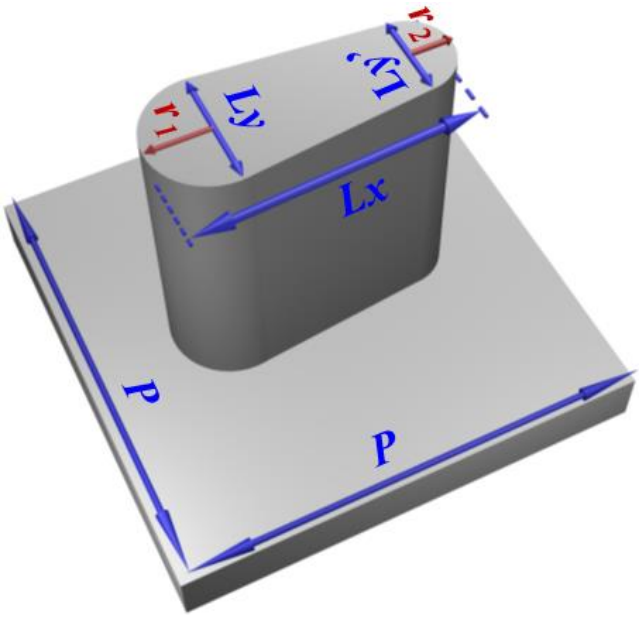

Figure S2. Schematic of the nanoblock geometry.

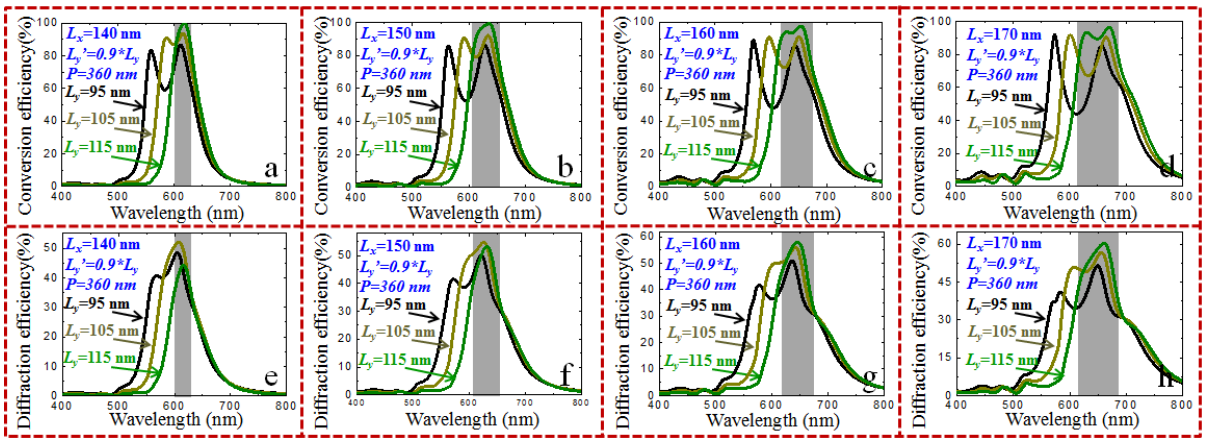

Figure S3. The conversion efficiency and diffraction efficiency of nanoblocks with various structure parameters for filtering red light.

In the simulation, the length of the nanoblock is changed from 140 (90) nm to 170 (120) nm, while the width is changed from 95 (65) nm to 115(85) nm for filtering red (green) light. P=360 nm, L_y'=0.9L_y, r_1=0.5L_y, and r_2=0.5L_y'. The numerical calculation of the conversion efficiency and diffraction efficiency is carried out by using the commercial microwave software CST Microwave Studio.

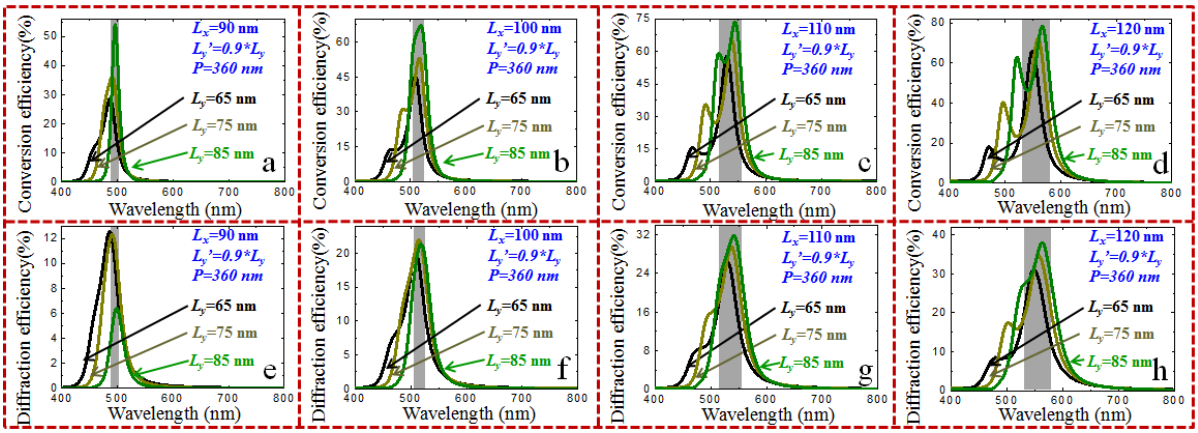

Figure S4. The conversion efficiency and diffraction efficiency of nanoblocks with various structure parameters for filtering green light.

Figs. S3 show the polarization purity (conversion efficiency) and diffraction efficiency of nanoblocks with different structure parameters. In Figs. S3(a) ~ S3(d), the response wavelength is gradually tuned from 600 to 680 nm when L_x (L_y) is changed from 140 (95) nm to 170 (115) nm, which means that the large nanoblock in the sample can perfectly filter red light in a wide change. The conversion efficiency (peak value) in this case is more than 80% in the range of the parameter variation. The response width becomes wider. The corresponding diffraction efficiency is depicted in Figs. S3(e)~S3(h). It shows the same variation tendency with a diffraction efficiency over 40%. For the green light filtering, the length and width of the nanoblocks are also changed with a variation range of 30 nm and 20 nm, respectively, as shown in Figs. S4(a)~S4(h). The response wavelength is in the range of 490~575 nm for L_x (L_y) when it is changed from 90 (65) nm to 120 (85) nm. Our simulation results show that the metasurface exhibit color filtering functionality, but the peak conversion efficiency and diffraction efficiency are lower than the case of perfect structure parameters.

Section 3 Malus' Law and color image encoding

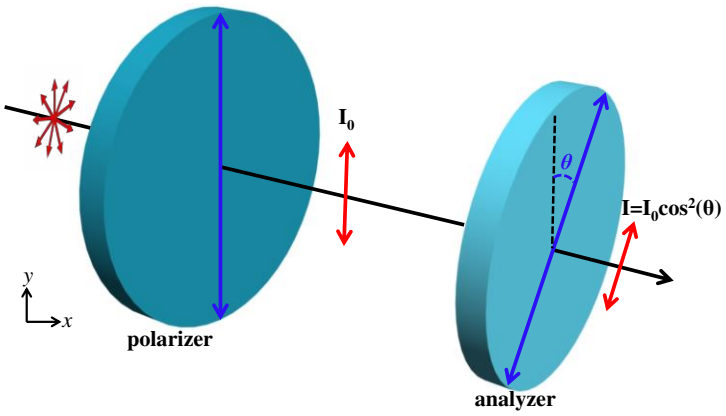

Figure S5. Schematic of the Malus' Law.

The schematic of the Malus' Law is depicted in Fig. S5. When a light beam is incident on the polarizer, a linearly polarized light beam with an intensity I_0 is generated (see Fig. S5). After the completely polarized light passes through the analyzer, the light intensity can be written as:

$$I = I_0 \cos^2 \theta, \tag{4}$$

Where θ is the angle between the transmission axes of the polarizer and the analyzer. The transmitted intensity of light after the analyzer is proportional to the square of the cosine of the angle θ, meaning that the transmitted intensity of a light beam can be modulated by controlling the angle θ.

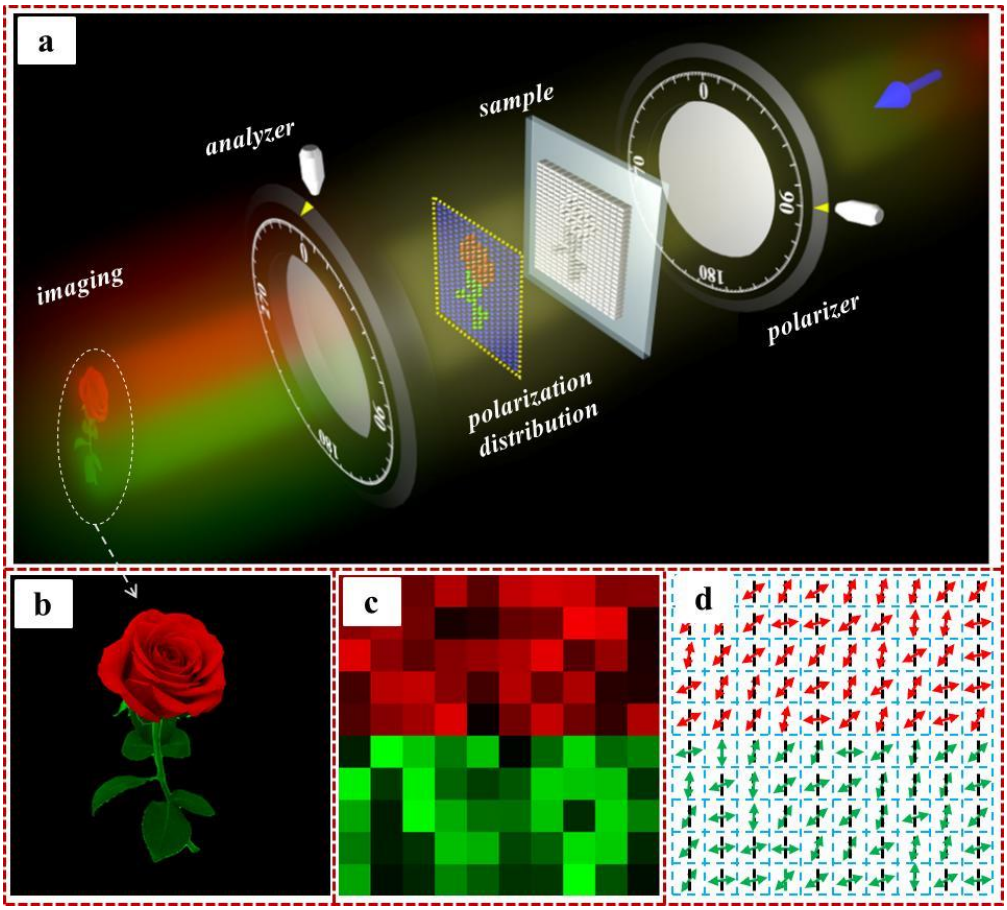

Figure S6. Mechanism of polarization encoding and decoding. (a) Schematic of the experimental setup. (b)The target image of a rose with green leaves. (c) Part of image with spatial distribution of brightness and color and (d) the corresponding desired polarization distribution. The green and red arrows represent the wavelength-dependent polarization states with different polarization orientations (red and green arrows for the wavelength at λ=665nm and λ=550nm, respectively).

Figure S6(a) shows the schematic of encoding and decoding process for a high-resolution color image based on Malus' Law. A light beam with a spatially inhomogeneous state of

polarization is generated upon the illumination of a linearly polarized light generated by the polarizer. An analyzer with a transmission axis perpendicular to that of the polarizer is used to reveal the hidden color image (see Fig. S6(b)). Figure S6(c) shows the part of the color image with spatial distribution of brightness and color. We select an area from the image with 10×10 pixels. Each pixel corresponds to a specific polarization state (see Fig. S6(d)). An inhomogeneous of intensity distribution of the target image is revealed after passing through the analyzer. The sample consists of 1200×1200 nanoblocks, meaning that the target image with same pixels is encoded into the polarization profile of the light beam [R2]. In addition, the dielectric-based anisotropic nanoblock (with different dimensions along x- and y-axis) is a wavelength-selective element. Wavelength-dependent polarization states (see the green and red arrows) can be generated and embedded into the light beam by optimizing the nanoblocks with different feature sizes.

Section 4. Material parameters and SEM images.

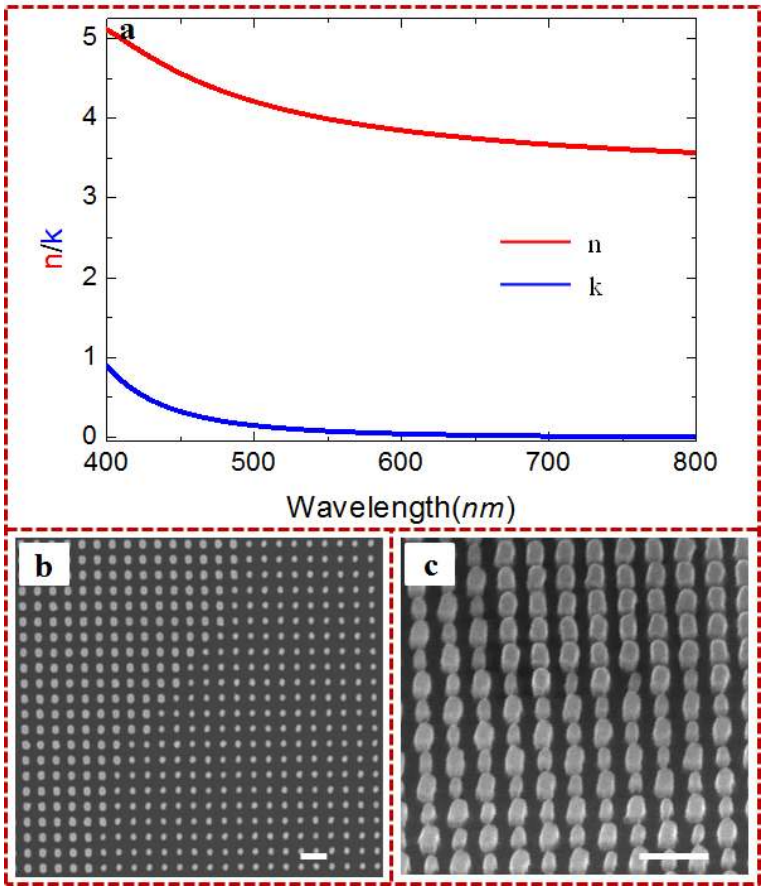

Figure S7. The refractive index of the amorphous silicon film with a thickness of 310 nm and the SEM images of the fabricated samples. (a) Red and blue curves represent the real and imaginary parts of the refractive index, respectively. (b) SEM image of the flower sample. (c) SEM image of the fruit sample with a tilt angle. The scale bar in (b) and (c) is 500 nm.

Figure S7(a) shows the real and imaginary parts of the refraction index of the amorphous silicon film with a thickness of 310 nm. The samples consist of the amorphous silicon nanoblocks on the quartz substrates. The scanning electron microscope (SEM) images of samples are shown in Figs. S7(b) and S7(c) (with a tilt angle), respectively.

Section 5. Broadband response of silicon nanoblocks

The designed silicon nanoblocks respond to the broadband incident light (see Fig. S8). Figures S8(a)～S8(g) show the experimental results under the illumination of green light with wavelengths ranging from 535 nm to 565 nm. The green leaves (without the obvious green flower) respond to wavelengths between 545 nm and 560 nm. Only the red flower is captured at the wavelengths ranging from 610 nm to 700 nm, as shown in Figs. S8(h)～S8(q). When an incident light beam containing two colors (red and green) shines on the fabricated metasurface device, a high-resolution full-color-like image is revealed (see Figs. S8(r)～S8(t)). For λ_1=550 nm (or λ_1=565 nm) and λ_2=660 nm (or λ_2=610 nm), a vivid rose is revealed onto the detector, indicating that our designed silicon nanoblocks respond to a broadband regime.

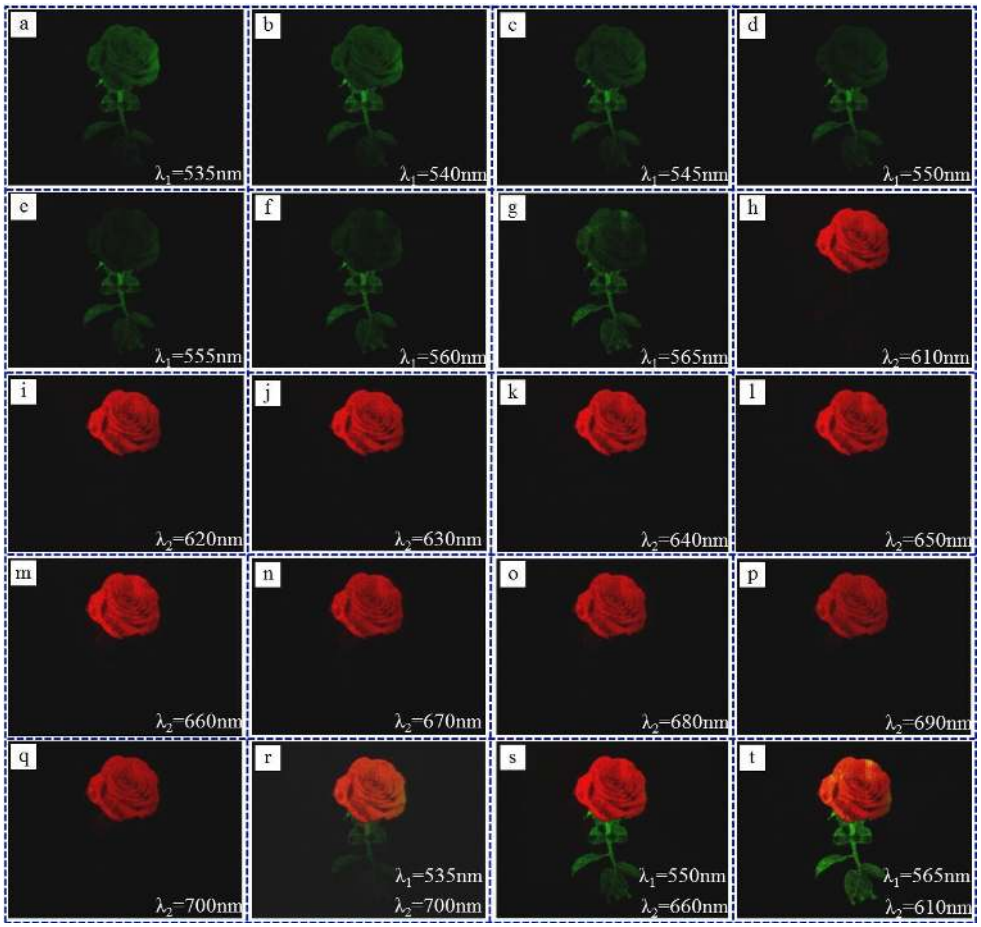

Figure S8. The revealed color images under the illumination of linearly polarized green light, red light and their combination.

Section 6. The developed metasurfaces devices for encryption

No images can be observed from the transmitted beam if the required analyzer is not used (see Figs. S9(a) and S9(c)). In stark contrast to the case with an analyzer, fine details of the images are clearly observed (see Figs. S9(b) and S9(d)) due to the presence of the brightness and color information, indicating the great potential of this technique for encryption application. For example, the petals of the red flowers and the leaf veins in Fig. S9(b) are observed while no images are obtained without the analyzer. Here, it should be noted that in order to reveal the color image and remove the background information (based on Malus' Law), the transmission axes of the polarizer and analyzer are set along *y*- and *x*-axis, respectively.

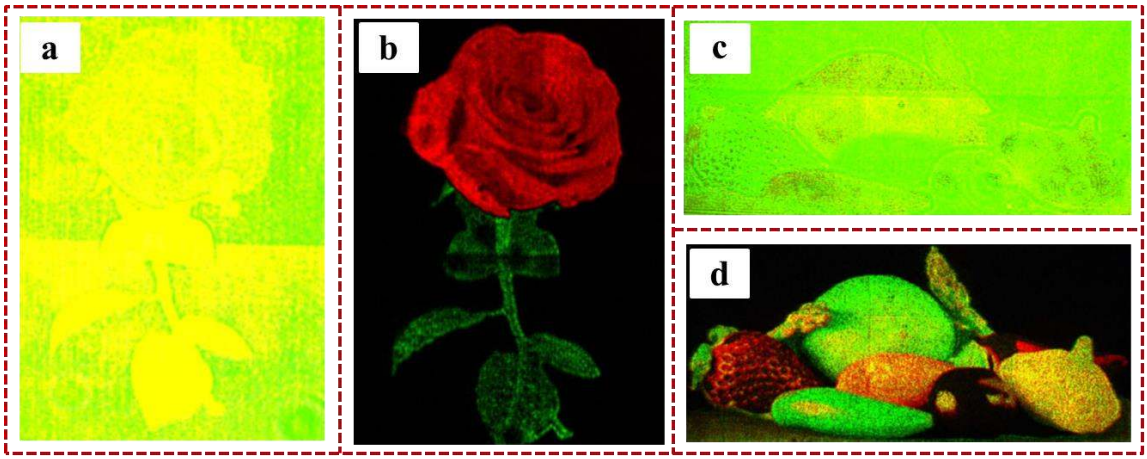

Figure S9. Measured results without and with the required analyzer. (a) and (c) no images are obtained without an analyzer, while (b) and (d) the hidden images are revealed with it.

Section 7. The conversion efficiency spectrum and optical energy distributions for RG model

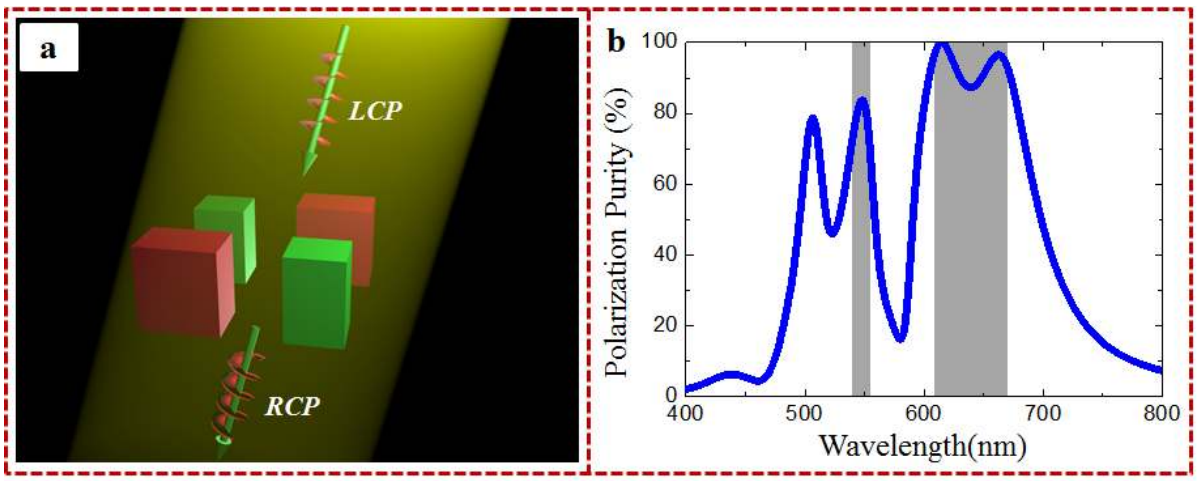

Figure S10. Conversion efficiency spectrum for supercell. (a) Calculation model for the supercell; (b) the corresponding conversion efficiency.

Each supercell contains four nanoblocks of two different types, where two nanoblocks of each type are positioned diagonally. Each type of intertwined nanoblocks respond to a specific wavelength upon the illumination of a light beam containing red and green colors (see Fig. S10(a)). The numerical calculations for the conversion efficiency under the LCP illumination and RCP transmission is shown in Fig. S10(b). In the high frequency regime, the supercell responds to the wavelength at λ=550nm, while in the low frequency it operates in a broadband regime ranging from 610 nm to 670 nm with a conversion efficiency over 90%. Such a supercell shows high efficiency (>80%) at the wavelengths of λ_1=550 nm and λ_2=660 nm, which is desirable for color mixing.

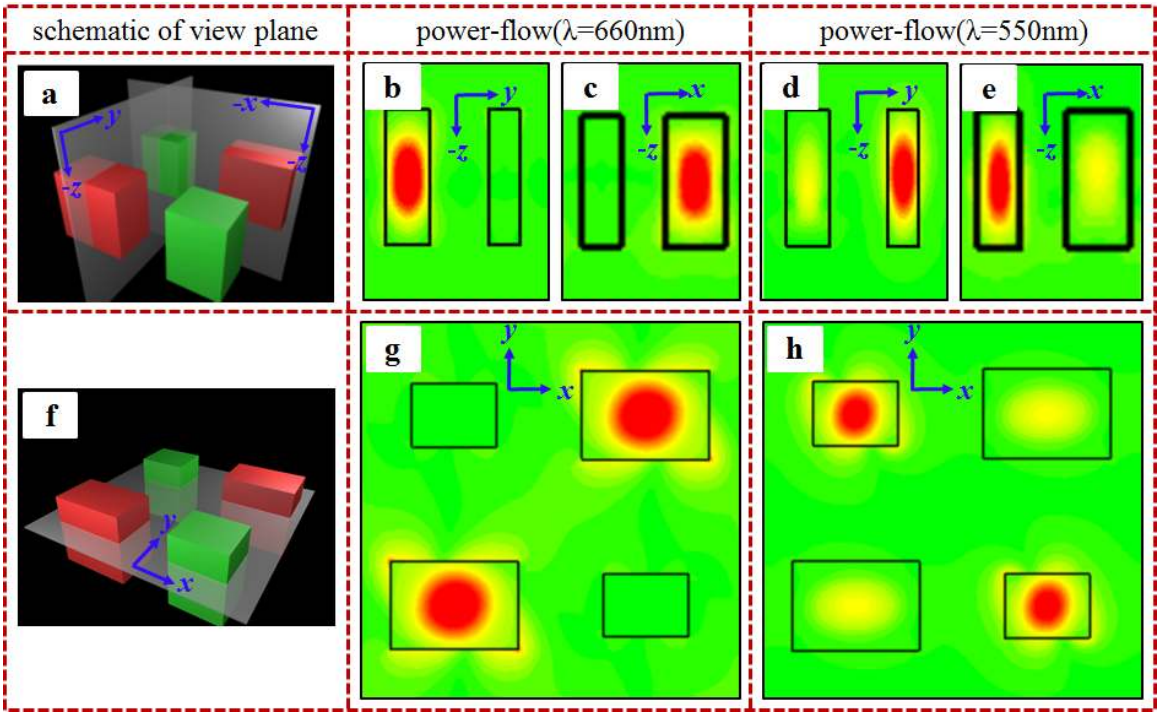

Figure S11. The calculated optical energy distributions without considering the substrate. (a) and (f) are the schematics of the view plane. (b) and (c) are the power-flow at *y*-*z* and *x*-*z* plane, respectively for λ=660 nm, while (d) and (e) are the corresponding power-flow for λ=550 nm. (g) and (h) are the power-flow at *x*-*y* plane for λ=660 nm and λ=550 nm, respectively. The scattering properties are slightly affected since the substrate is not considered.

To further demonstrate the frequency-selective characteristics of the designed super-cell, we show the corresponding optical energy distributions based on the full wave simulations (see Fig. 11). Supplementary Figs. 11(a) and 11(f) show the schematics of the view plane. For λ=660 nm, the incident optical energy is totally located onto these two large nanoblocks of the supercell (see Figs. 11(b), 11(c) and 11(g)), while the small nanoblocks are resonant at λ=550nm (see Figs. 11(d), 11(e) and 11(h)). Therefore, these two types of nanoblocks can be

considered as two wavelength-dependent color filters. Each nanoblock corresponds to a color-dependent pixel, and the color mixing is realized by rotating the nanoblocks to modulate the ratio of two colors to generate additive color mixing.

Section 8. Optical measurement under the illumination of white light.

We also perform optical measurement with white light source (Dolan-Jenner MI-150 Fiber Optic Illuminator) (Fig.S12(a)). Fig. S12(b) and S12(c) show the observed experimental results for the flower and fruit samples, respectively. For the full-color-like image, eight different types of high-resolution fruits with different colors are also revealed. The experimental results clearly show that the developed metasurface surface can operate under the illumination of white continuum light, which indicates the robustness of the proposed approach and fabricated metadevices.

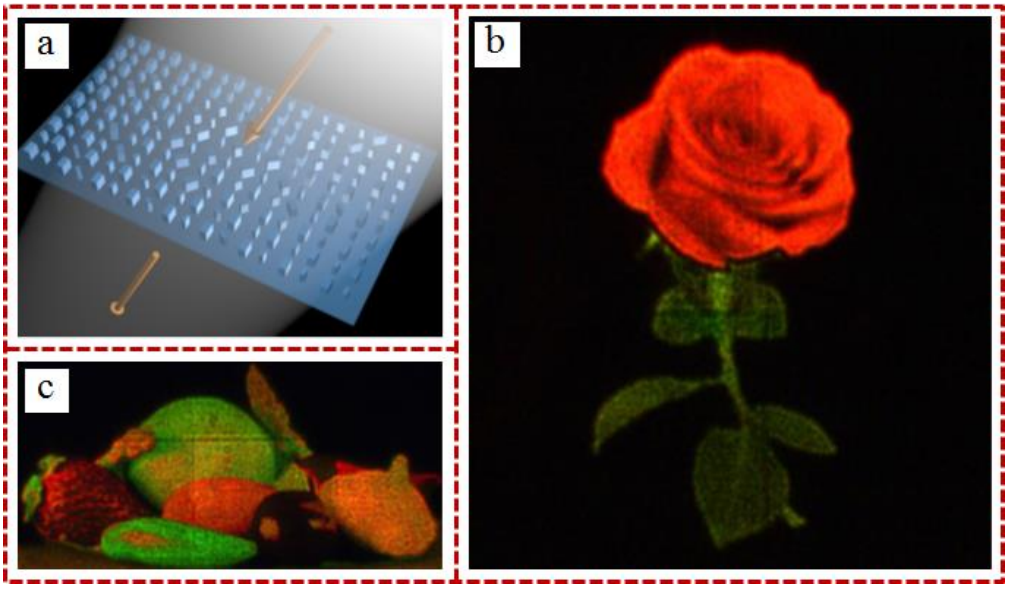

Figure S12. (a) Schematic of optical measurement under the illumination of white continuum light. (b) and (a) are the measured results for rose and fruit samples, respectively.

Section 9. Conversion efficiency and diffraction efficiency

Figure S13(a) and S13(b) shows the theoretical conversion efficiency and diffraction efficiency of the designed nanoblocks with two different geometrical structures (one for red, one for green). For L_x=100 nm (150 nm), L_y=75 nm (105 nm), the simulated conversion efficiency is over 60% (90%) with a wavelength range from 535 nm (630 nm) to 560 nm (670 nm), while the diffraction efficiency is over 23% (40%) (see Figs. S13(a) and S13(b)). To perform optical measurement, we fabricated two metasurfaces consisting of nanoblocks with uniform orientations. The experimental results for the red and green color are shown in Fig. S13(c) and S13(d), respectively. The experimental conversion efficiency is more than 70%

(70%) ranging from 560 nm (670 nm) to 578 nm (695 nm), which indicates the high polarization purity (conversion efficiency) of the light. In comparison with the simulation results, the red shift of response wavelength is mainly to the fabrication error, in which the lateral size of fabricated nanoblocks are larger than the designed ones. However, the response wavelengths for encoding the color images (flower and fruit) are much closer to the designed values of 550 nm and 660 nm, which is evidenced by the obtained experimental results under the illumination of white light (Fig. S12).

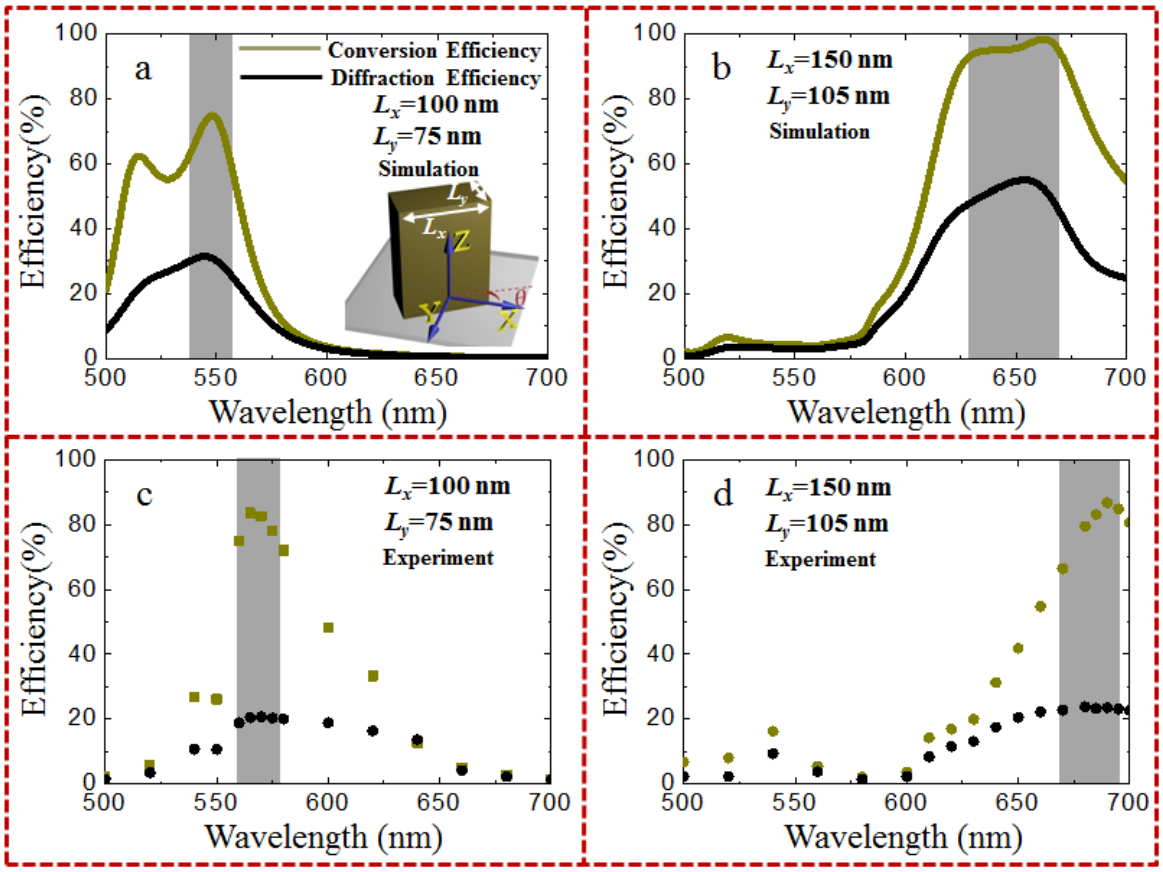

Figure S13. Conversion efficiency (dark yellow line/dot) and diffraction efficiency (black line/dot) for the nanoblocks with two different geometrical structures: (a) and (c) with L_x=100 nm, L_y=75 nm; (b) and (d) with L_x=150 nm, L_y=105 nm. The first row and second row represent the simulated and experimental results, respectively. Inset is the simulation model.

Section 10. The conversion efficiency and optical energy distributions for RGB model

Figure S14 shows the calculated conversion efficiency spectrum and optical energy distributions of the supercell that can filter the red, green and blue colors. The supercell consists of three types of nanoblocks (see Fig. S14(a)) with corresponding structure parameters as follows: L_{x1}=150 nm, L_{y1}=105 nm, L_{x2}=100 nm, L_{y2}=75 nm, L_{x3}=80 nm, L_{y2}=55

nm, and the period is 450 nm. Figure S14(b) depicts the numerical calculations for the transmission spectrum upon the illumination of LCP light with RCP transmission. Three peak wavelengths are located at 460 nm, 547 nm, and 660 nm, respectively, which are close to the central wavelengths of the three-primary colors. For λ=547 nm and 660 nm, the conversion efficiency is over 55%, while the conversion efficiency is about 25% at λ=460 nm, which is much lower than that of red and green pixels. The power-flow distributions are shown in Figs. S14(c)～S14(e). It should be noted that three kinds of nanoblocks correspond to wavelength-dependent color filters. Therefore, such supercell with different orientation of nanoblocks have the capability of color mixing between red, green and blue colors. Thus a full-color image can be realized based on the color mixing.

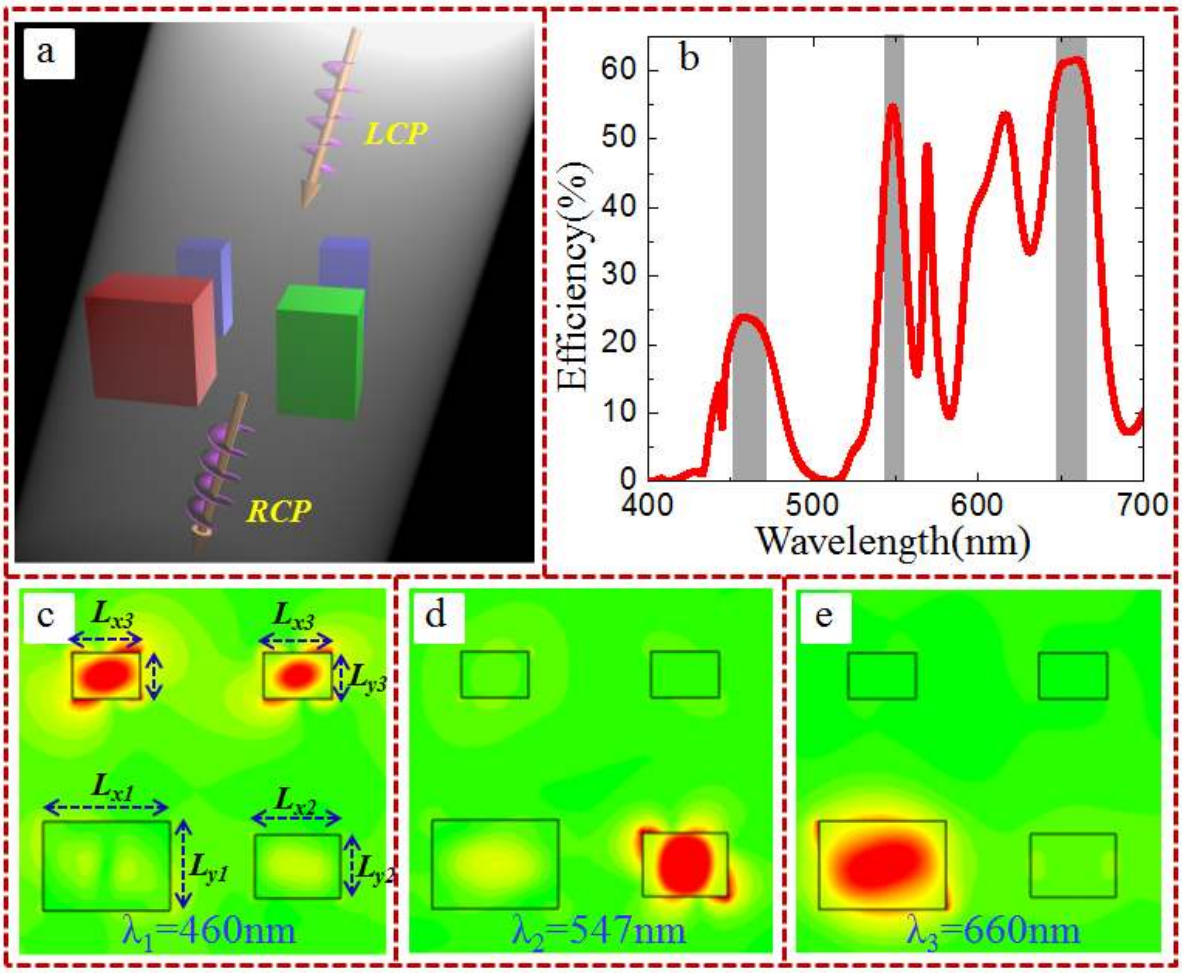

Figure S14. The calculated conversion efficiency and optical energy distributions for the supercell containing three types of nanoblocks. (a) calculation model for the supercell. (b) simulated conversion efficiency. (c), (d) and (e) are the corresponding power-flow for λ=465 nm, 547 nm and 660 nm, respectively.

References

R1. D. Goldstein. *Polarized light* (Marcel Dekker, 2003).

R2. F. Yue, C. Zhang, X. Zang, D. Wen, B. D. Gerardot, S. Zhang, X. Chen. High-resolution grayscale image hidden in a laser beam. *Light: Sci & Appl*. **2018**, 7, e17129.

R3. B. Wang, F. Dong, Q. T. Li, D. Yang, C. Sun, J. Chen, Z. Song, L. Xu, W. Chu, Y. F. Xiao, Q. Gong, Y. Li. *Nano. Lett*. **2016***, 16*, 5235-5240.